Supplementary Information

Tuning the drug multimodal release through a co-assembly strategy based on magnetic gels

Sérgio R. S. Veloso[1], Ecem Tiryaki[2], Carlos Spuch[3], Loic Hilliou[4], C. O. Amorim[5], V. S. Amaral[5], Paulo J. G. Coutinho[1], Paula M. T. Ferreira[6], Verónica Salgueiriño[2,7], Miguel A. Correa-Duarte[7,*], and Elisabete M. S. Castanheira[1,*]

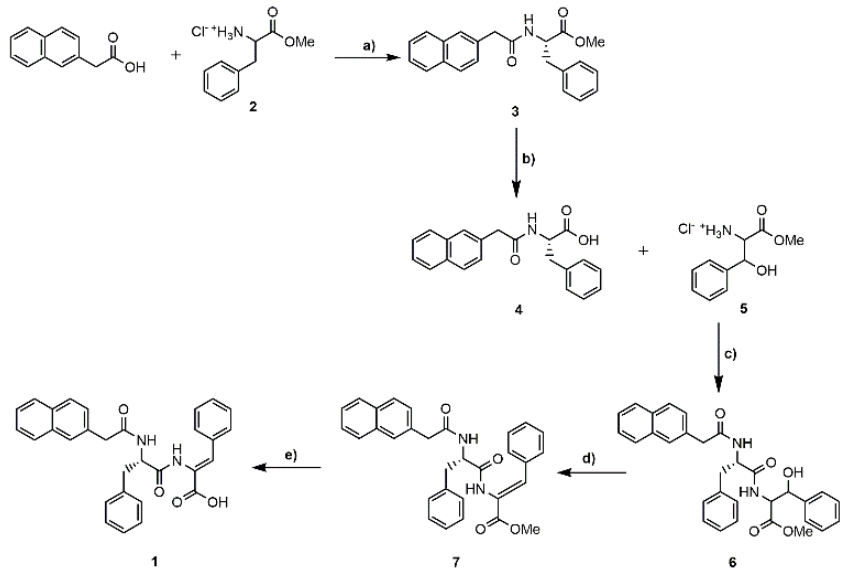

Scheme 1. Synthesis of compound **1**. a) DCC, HOBt, Et_3N, ACN, rt; b) (1) NaOH (1 M), methanol, rt, (2) $KHSO_4$; c) DCC, HOBt, Et_3N, ACN, rt; d) (1) Boc_2O, DMAP, dry ACN, rt (2) TMG; e) (1) NaOH (1 M), 1,4-dioxane, rt, (2) $KHSO_4$.

Synthesis of the methyl ester of phenylalanine [H-D,L-Phe-OMe (2)]: Phenylalanine [H-D,L-Phe-OH] (31.8 mmol, 5.26 g) was added to methanol for a final concentration of 1 M in an ice bath. Thionyl chloride (3.4 equiv) was added dropwise and the reaction mixture was left stirring for 8 h at 40 °C. The solvent was removed under reduced pressure and ethyl ether was added. The process was repeated until a white solid of compound **2** was formed. (98%, 6.72 g).

^{1}H NMR (400 MHz, DMSO-d6) δ: 3.09 (1H, dd, J = 7.4 and 14.0 Hz, *β*-CH), 3.20 (1H, dd, J = 5.6 and 14.0 Hz, *β*-CH), 3.64 (3H, s, OCH_3), 4.22 (1H, t, J = 6 and 7.4 Hz, *α*-CH), 7.22-7.34 (5H, m, Ar H), 8.74 (3H, s, NH^{3+}).

Synthesis of the methyl ester of *N*-2-naphtylacetyl-L-phenylalanine [2-Nap-L-Phe-OMe (3)]: 2-Naphthylacetic acid (0.93 g, 5 mmol) was dissolved in acetonitrile (10 mL $mmol^{-1}$) and put in an ice bath. HOBt (1.10 equiv), DCC (1.10 equiv), H-D,L-Phe-OMe (1.10 equiv), and triethylamine (2.10 equiv) were added with 2 min between each addition. The mixture was left stirring at rt overnight. The urea was

filtered, and the solvent removed under reduced pressure. Acetone was added, and the mixture was stored in the freezer for 2 h. The urea was filter again. Evaporation at reduced pressure gave a residue that was partitioned between ethyl acetate (30 mL) and $KHSO_4$ (30 mL, 1M). The organic phase was thoroughly washed with $KHSO_4$ (1M, 2 x 30 mL), $NaHCO_3$ (1M, 2 x 30 mL) and brine (3 x 30 mL) and dried with $MgSO_4$. Removal of the solvent afforded compound **3** (95%, 1.65 g).

^{1}H NMR (400 MHz, $CDCl_3$) δ: 3.01 (2H, dq, J = 5.6 and 14.0 Hz, *β*-CH_2), 3.70 (3H, s, OCH_3), 3.72 (2H, s, CH_2), 4.84-4.88 (1H, m, *α*-CH), 5.83 (1H, d, J = 7.2 Hz, NH), 6.78-6.81 (2H, m, ArH Phe), 6.99 (2H, t, J = 8.0 Hz, ArH Phe), 7.10 (1H, tt, J = 2.0 and 7.4 Hz, ArH Phe), 7.3 (1H, dd, J = 1.6 and 8.4 Hz, ArH Naph), 7.49-7.54 (2H, m, ArH Naph), 7.66 (1H, s, H Naph), 7.79-7.87 (3H, m, ArH Naph).

Synthesis of *N*-2-naphtylacetyl-L-phenylalanine [2-Nap-L-Phe-OH (4)]: The Nap-L-Phe-OMe (1.65 g, 4.75 mmol) was dissolved in methanol (10 mL $mmol^{-1}$) and a solution of NaOH 1 M (1.5 equiv) was added. The reaction was followed by TLC until no starting material was detected. The organic solvent was removed under reduced pressure, and the reaction mixture was acidified to pH 2-3 with $KHSO_4$ (1 M). The solid was filtered and washed with ethyl ether. The solid was identified as 2-Nap-L-Phe-OH, **4** (1.4 g, 91 %).

^{1}H NMR (400 MHz, DMSO) δ: 2.84-2.90 (1H, m, *β*-CH_2), 3.04-3.08 (1H, m, *β*-CH_2), 3.53-3.62 (2H, m, CH_2), 4.39-4.44 (1H, m, *α*-CH), 7.18 (5H, s, ArH), 7.25-7.28 (1H, dd, J = 1.6 and 8.4 Hz, ArH), 7.43-7.49 (2H, m, ArH), 7.64 (1H, s, ArH), 7.76-7.80 (2H, m, ArH), 7.84-7.86 (1H, d, J = 8.0 Hz, ArH), 8.38 (1H, d, J= 8.0 Hz, NH), 12.60 (1H, s, CO_2H);

Synthesis of the methyl ester of *β*-hydroxyphenylalanine [H-D,L-Phe(*β*-OH)-OMe (5)]: The *β*-hydroxyphenylalanine [H-D,L-Phe(*β*-OH)-OH] (30 mmol, 5.44 g) was added for a final concentration of 1 M in an ice bath. Thionyl chloride (3.4 equiv) was added dropwise and the reaction mixture was left stirring for 8 h at 40 °C. The solvent was removed under reduced pressure and ethyl ether was added. The process was repeated until a white solid of compound **5** was formed (98%, 5.74 g).

^{1}H NMR (400 MHz, DMSO) δ: 3.60 (3H, s, OCH_3); 4.15 [1H, d, α-CH Phe(*β*-OH)]; 5.01-5.02 [1H, t, *β*-CH Phe(*β*-OH)]; 6.56 [1H, brs, J = 4.4 Hz, OH Phe(*β*-OH)]; 7.31-7.38 [5H, m, ArH Phe(*β*-OH)]; 8.45 [3H, s, NH_3^+ Phe(*β*-OH)].

Synthesis of the methyl ester of *N*-2-naphtylacetyl-L-phenylalanine-*β*-hydroxyphenylalanine [2-Nap-L-Phe-D,L-Phe(*β*-OH)-OMe (6)]: Nap-L-Phe-OH (1.4 g, 4.2 mmol) was dissolved in acetonitrile (10 mL $mmol^{-1}$) and put in an ice bath. HOBt (1.10 equiv), DCC (1.10 equiv), H-D,L-Phe-OMe (1.10 equiv), and triethylamine (2.10 equiv) were added with 2 min between each addition. The mixture was left stirring

at rt overnight. The urea was filtered, and the solvent removed under reduced pressure. Acetone was added, and the mixture was stored in the freezer for 2 h. The urea was filter again. Evaporation at reduced pressure gave a residue that was partitioned between ethyl acetate (30 mL) and $KHSO_4$ (30 mL, 1M). The organic phase was thoroughly washed with $KHSO_4$ (1M, 2 x 30 mL), $NaHCO_3$ (1M, 2 x 30 mL) and brine (3 x 30 mL) and dried with $MgSO_4$. Removal of the solvent afforded compound **6** as a diastereomeric mixture (76.1%, 1.63 g).

^{1}H NMR (400 MHz, $CDCl_3$) δ: 2.6-2.7 (1H, m, *β*-CH Phe), 2.80-2.85 (2H, m, 2×*β*-CH Phe), 2.9 (1H, m, *β*-CH Phe), 3.61 (4H, s, 2×CH_2 Naph), 3.69 [6H, s, 2×OCH_3 Phe(*β*-OH)], 4.66-4.83 [4H, m, 4×*α*-CH Phe and Phe(*β*-OH)], 5.22 [1H, d, J = 3.2 Hz, *β*-CH Phe(*β*-OH)], 5.28 [1H, d, J = 3.2 Hz, *β*-CH Phe(*β*-OH)], 5.88 (1H, m, NH), 5.99 (1H, m, NH), 6.60-6.64 (2H, m, ArH), 6.80-7.34 (22H, m, 16×ArH, 2×NH), 7.40-7.6 (6H, m, ArH), 7.7-7.9 (6H, m, ArH).

Synthesis of the methyl ester of *N*-2-naphtylacetyl-L-phenylalanine-*Z*-dehydrophenylalanine [2-Nap-L-Phe-Z-ΔPhe-OMe (7)]: To a solution of compound **6** in dry acetonitrile (10 mL, 1 M) DMAP (0.1 equiv) and Boc_2O (1 equiv) were added under rapid stirring at rt. The mixture was monitored by ^{1}H NMR until all reactant was consumed. *N,N,N',N'*- tetramethylguadinine (2 % in volume, 0.2 mL) was added under continued stirring. The mixture was left stirring at rt and monitored by ^{1}H NMR until all reactant was consumed. The precipitate was filtered and identified as compound **7** (0.99 g, 63%).

^{1}H NMR (400 MHz, $CDCl_3$) δ: 2.94-3.01 (2H, m, *β*-CH_2 Phe), 3.68 (2H, s, CH_2 Naph), 3.80 (3H, s, OCH_3), 4.78-4.84 (1H, m, α-CH), 5.92 (1H, d, J = 7.6 Hz, NH Phe), 6.97-7.18 (6H, m, 6×ArH), 7.27-7.38 (7H, m, 7×ArH), 7.50-7.56 (2H, m, ArH and *β*-CH ΔPhe), 7.75-7.86 (4H, m, 3×ArH and NH ΔPhe).

Synthesis of the *N*-2-naphtylacetyl-L-phenylalanine-*Z*-dehydrophenylalanine [2-Nap-L-Phe-*Z*-ΔPhe-OH (1)]: Compound **7** (0.99 g, 2.3 mmol) was dissolved in 1,4-dioxane (10 mL mmol^{-1}) and a solution of NaOH 1 M (3 equiv) was added. The reaction was followed by TLC until no starting material was detected. The organic solvent was removed under reduced pressure, and the reaction mixture was acidified to pH 2-3 with $KHSO_4$ (1 M). The solid was filtered and washed with ethyl ether. The solid was identified as 2-Nap-L-Phe-*Z*-ΔPhe-OH, **1** (1.02 g, 90 %).

^{1}H NMR (400 MHz, DMSO) δ: 2.77-2.83 (1H, m, *β*-CH), 3.12-3.17 (1H, m, *β*-CH), 3.54-3.62 (2H, m, CH_2 Naph), 4.58-4.63 (1H, m, *α*-CH Phe), 6.96 (1H, s, *β*-CH ΔPhe), 7.05-7.46 (13H, m, Ar H), 7.62 (1H, s, Ar H), 7.71-7.85 (3H, m, Ar H), 8.59 (1H, d, J = 8.8 Hz, NH Phe), 9.73 (1H, s, NH ΔPhe);

^{13}C NMR (100.6 MHz, DMSO) δ: 37.16 (*β*-CH_2 Phe), 42.18 (CH_2 Naph), 54.14 (*α*-CH Phe), 125.43 (CH), 125.95 (CH), 126.27 (CH), 126.54 (*α*-C ΔPhe), 127.19 (CH), 127.33 (CH), 127.41 (CH), 127.57 (CH), 128.02

(CH), 128.46 (CH), 129.18 (CH), 129.25 (CH), 129.93 (CH), 131.70 (C), 131.93 (*β*-CH ΔPhe), 132.89 (C), 133.54 (C), 133.94 (C), 137.85 (C Phe), 166.19 (C=O ΔPhe), 170.06 (C=O Phe), 171.16 (C=O Naph); HRMS (ESI) *m/z*: $[M+H]^+$ calcd for $C_{30}H_{27}N_2O_4^+$ 479.19653; found, 479.19627. Mp: 165.0-167.0 °C.

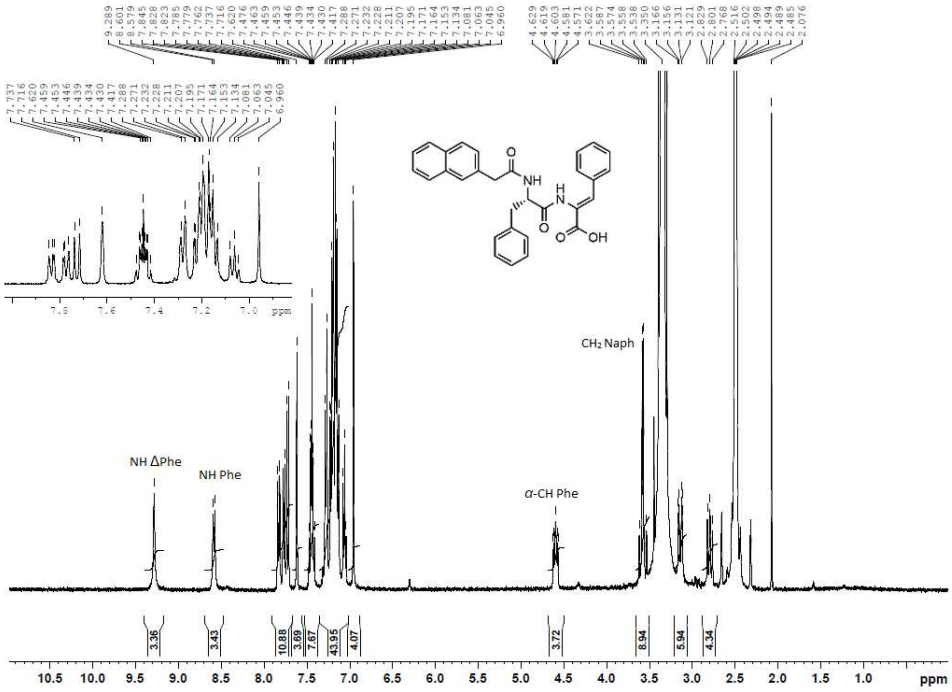

Figure S1. ^{1}H NMR spectrum of 2-Nph-L-Phe-*Z*-ΔPhe-OH, **1** in DMSO-d_6.

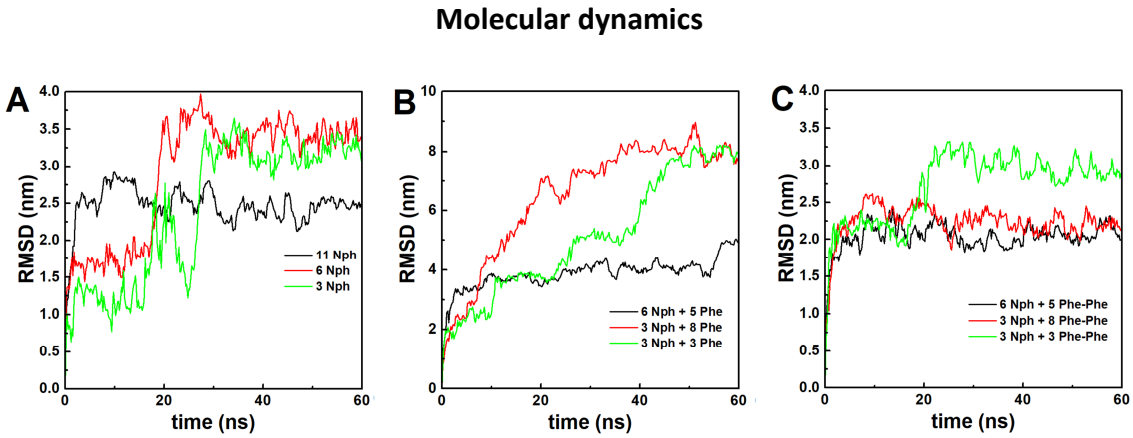

Figure S2. Root-mean-square deviation (RMSD) of the 2-Nph-L-Phe-*Z*-ΔPhe-OH (Nph) dehydropeptides without (A) and with (B) phenylalanine (Phe) and (C) diphenylalanine (Phe-Phe).

Figure S3. Molecular dynamics assays snapshots over the 60 ns. Legend: Nph: 2-Nph-L-Phe-*Z*-ΔPhe-OH (green); Phe: phenylalanine (blue); Phe-Phe: diphenylalanine (yellow).

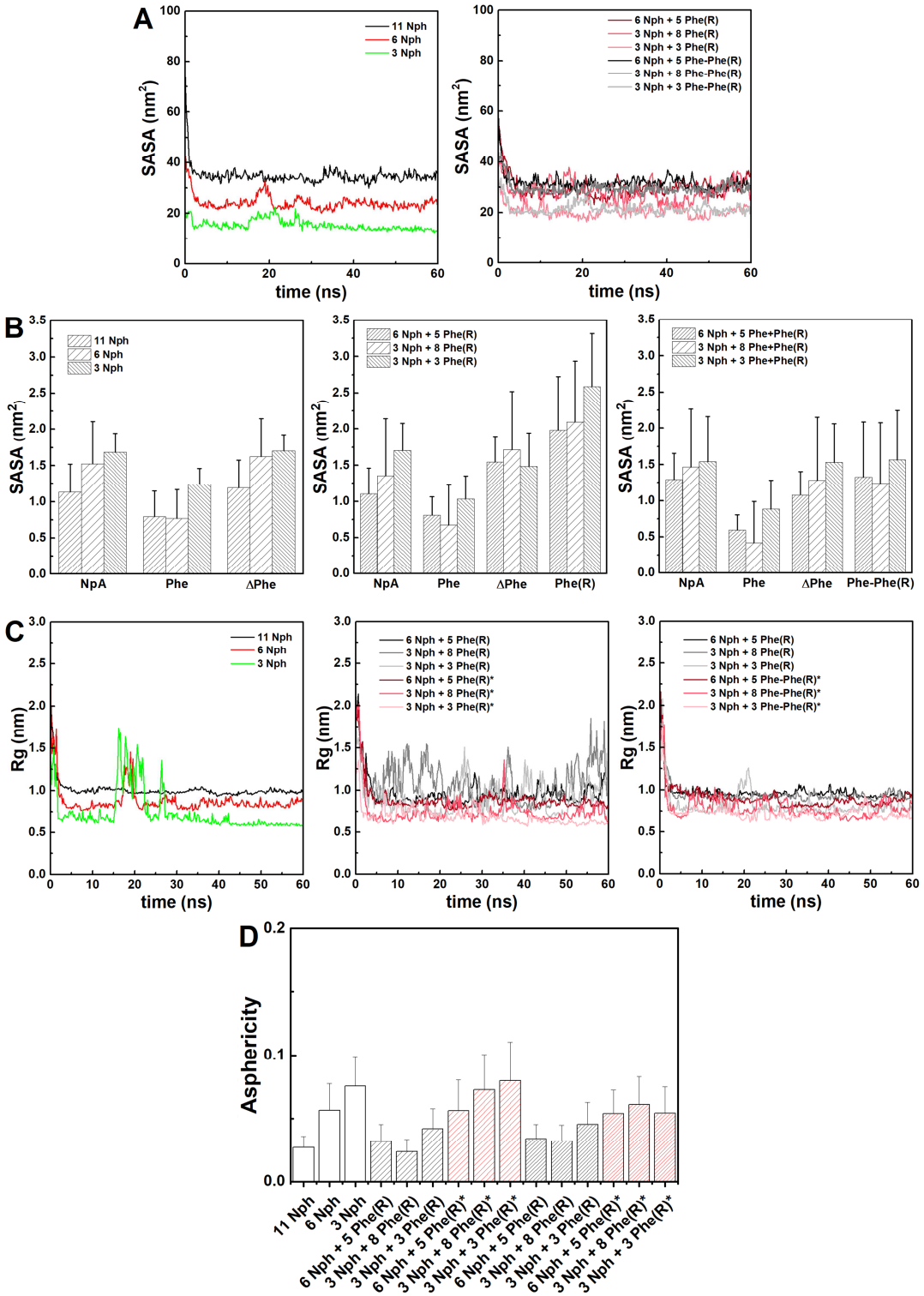

Figure S4. (A) Average solvated surface area over time of the systems. Legend: Nph: 2-Nph-L-Phe-*Z*-ΔPhe-OH; NpA: 2-naphtalene acid; Phe: phenylalanine; ΔPhe: Dehydrophenylalanine; Phe-Phe: diphenylalanine; "(R)": residue added. (B) Average solvated surface area of the dehydropeptide residues. (C) Radius of gyration of the aggregate over time. Legend: *: without phenylalanine contribution. (D) Asphericity of the aggregates averaged over the 60 ns of dynamic simulation. The asphericity is defined as $r_{gz}^2 - 0.5(r_{gx}^2 + r_{gy}^2)$, where r_{gz}^2, r_{gx}^2 and r_{gy}^2 are the ordered principal moments of the gyration tensor so that $r_{gz}^2 > r_{gy}^2 > r_{gx}^2$, which is zero for a spherical shape and aspherical for values higher than zero [40,41].

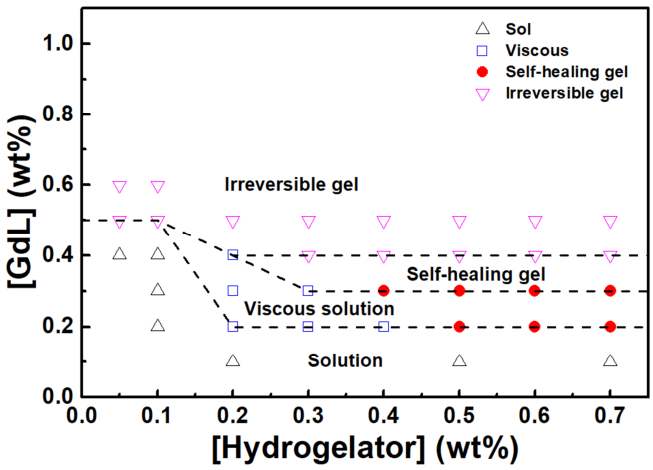

Figure S5. Phase transition diagram of the hydrogelator prepared through addition of GdL to a basic hydrogelator solution (2 v/v% NaOH 1M).

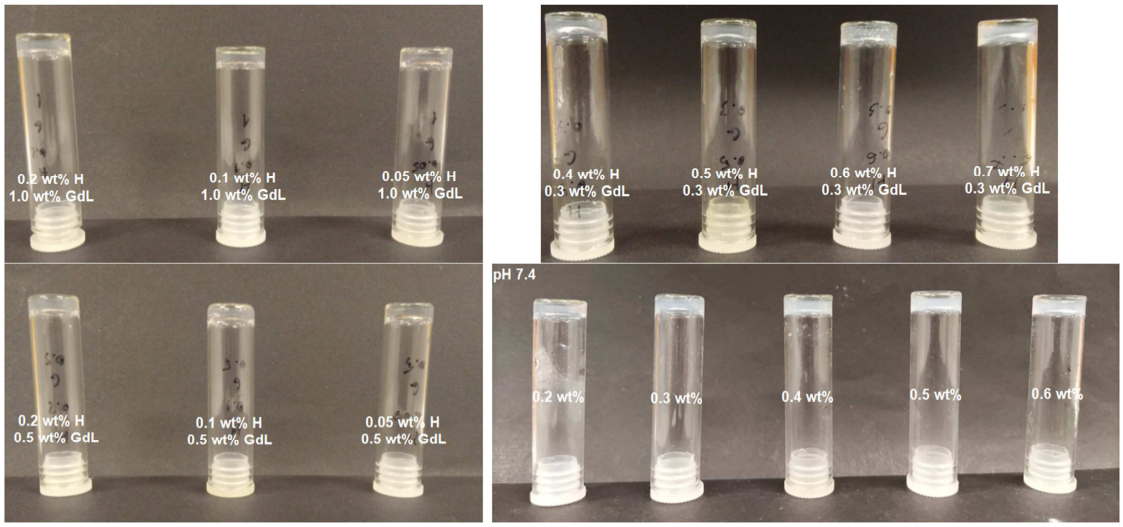

Figure S6. Images of hydrogels prepared through addition of GdL and through a heating-cooling cycle in pH 7.4 phosphate buffer.

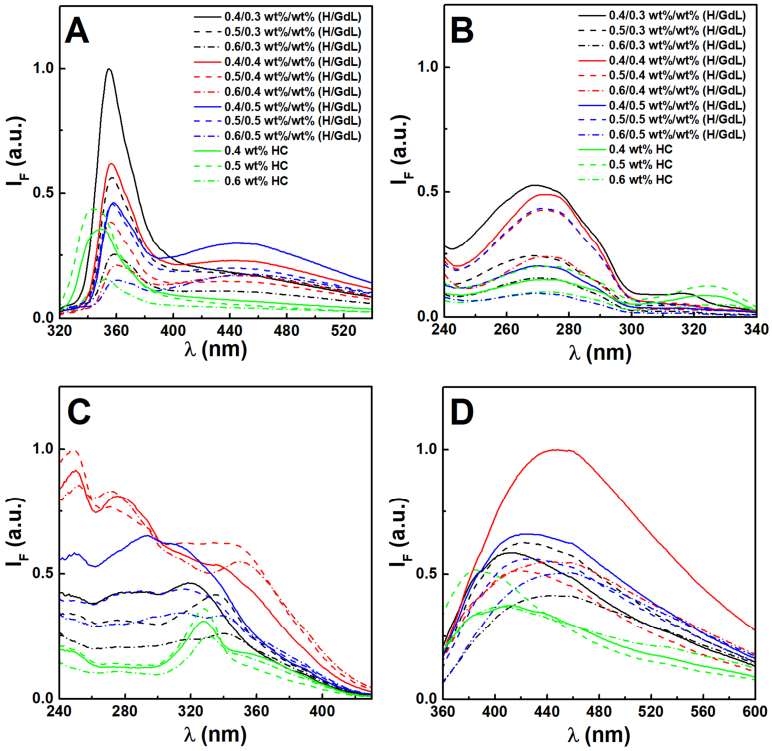

Figure S7. (A) Fluorescence emission spectra of hydrogels aromatic moieties directly excited (λ_{exc}=280 nm) at different hydrogelator-to-GdL ratios (H/GdL), and prepared through heating-cooling cycle (HC). Fluorescence excitation spectra of the (B) monomer band at 360 nm and (C) aggregates band at 450 nm at different hydrogelator-to-GdL ratios (H/GdL), and prepared through heating-cooling cycle (HC). (D) Fluorescence emission of the hydrogels aggregates through excitation at 340 nm. The difference in the excitation spectra of the bands centered at 360 nm and 450 nm demonstrate that different species contribute for each emission.

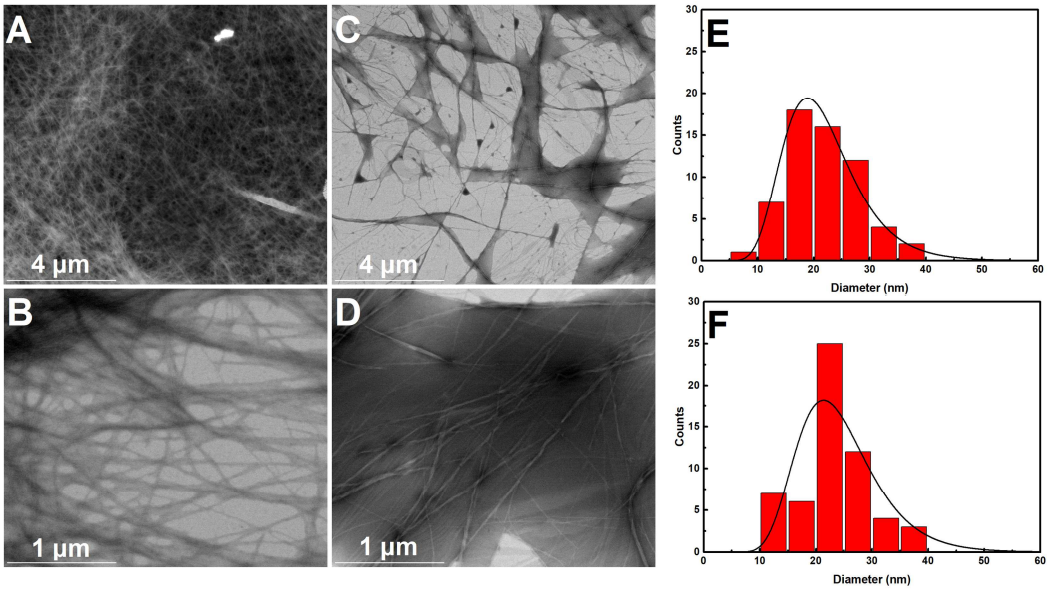

Figure S8. STEM images of hydrogels prepared at 0.5 wt% of hydrogelator through (A,B) the GdL (0.4 wt%) method and (C,D) heating-cooling cycle method (phosphate buffer pH=7.4). Size histograms of the hydrogels prepared through (E) GdL method and (F) heating-cooling cycle method fitted to a lognormal function.

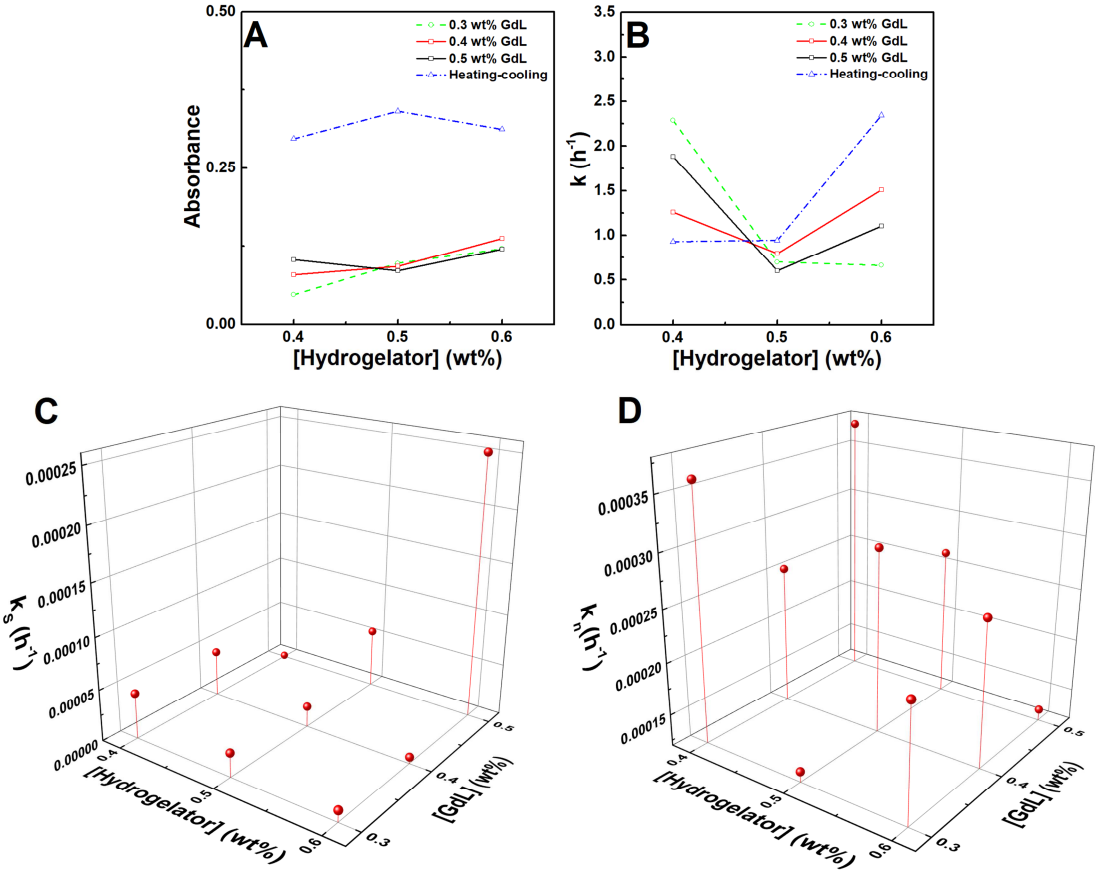

Figure S9. (A) Absorbance at 500 nm of hydrogels prepared through the GdL addition and heating-cooling cycle methods. (B) Dependence of the turbidity kinetics rate constant, k_{emp}, on the hydrogelator concentration obtained from the fitted sigmoidal model $T(t) = \frac{T(\infty)}{\sqrt[v]{(1+ve^{-k_{emp}(t-t_m)})}}$, where $T(t)$ is the turbidity at time t, $T(\infty)$ is the final turbidity, and t_m is the point of the maximum elongation rate (v is considered 1). (C,D) Kinetic parameters obtained from the fitting of the Saitô's fractional aggregation model to the fluorescence kinetics data. The parameter k_s is the effective growth rate, and k_n is the nucleation rate.

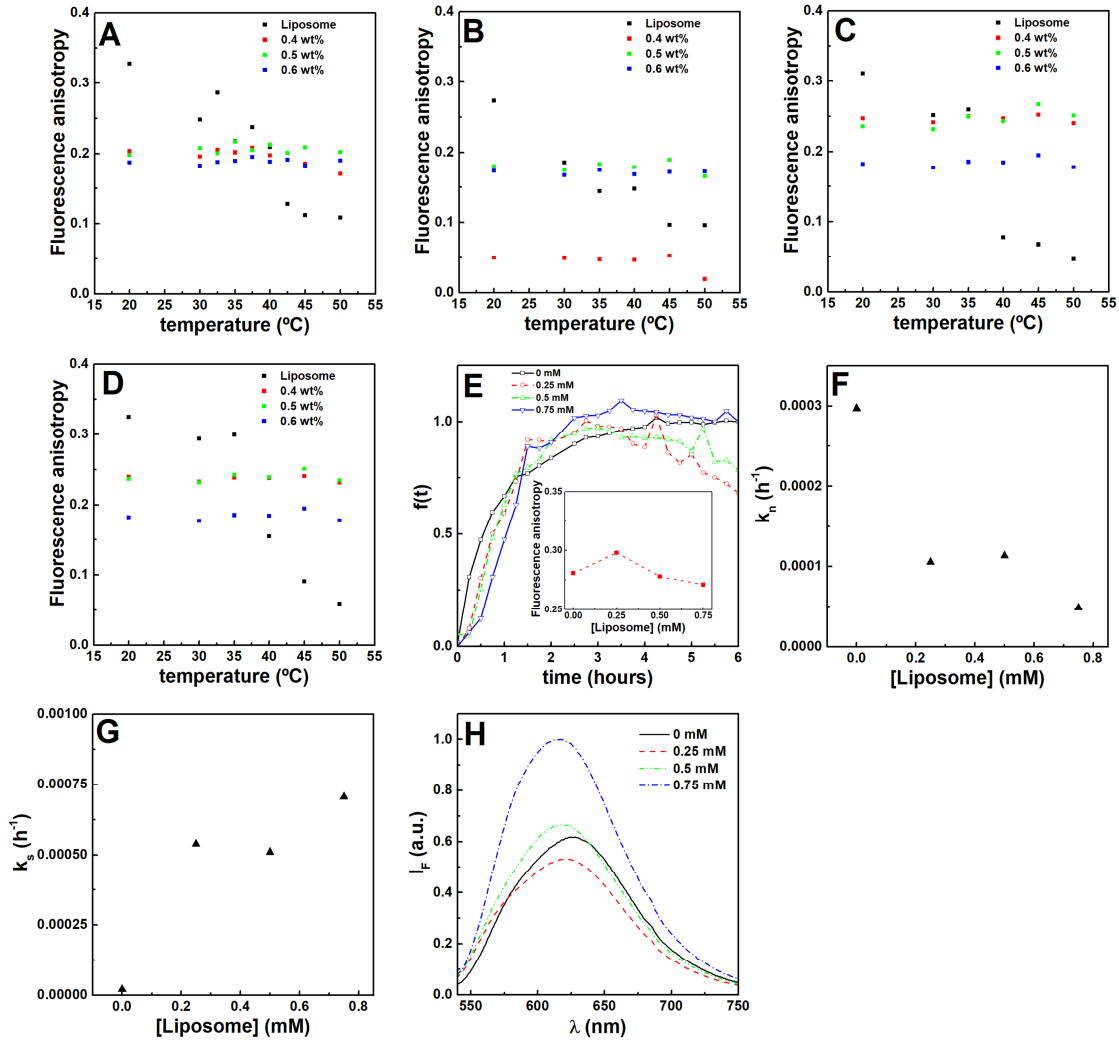

Figure S10. Temperature dependence of fluorescence anisotropy (*r*) of DPH (2 μM) loaded in liposomes of (A) DPPC, (B) PC:Ch (7:3), (C) DPPC:DOPG (9:1) and (D) DPPC:DOPE (9:1) incorporated in hydrogels at various concentration. (E) Fluorescence emission kinetics of hydrogel loaded with Nile Red (2 μM, λ_{exc}=520 nm, λ_{em}=620 nm) and various concentrations of liposomes. Inset: Nile Red fluorescence emission anisotropy dependence on DPPC:PEG (19:1) liposome content. (F,G) Nucleation (k_n) and effective growth (k_s) rate of fluorescence kinetics dependence on DPPC:PEG (19:1) liposome content in gels prepared at 0.5 wt% hydrogelator and 0.4 wt% GdL, and (H) the respective fluorescence emission of Nile Red (2 μM, λ_{exc}=520 nm, λ_{em}=620 nm).

Table S1. Hydrodynamic size (HD), polydispersity index (PDI), zeta potential of DPPC:Ch:PEG 17:2:1 and DPPC:PEG 19:1 liposome formulations at 25 °C and 45 °C. The doxorubicin fluorescence anisotropy (r) of the lipogel formulations was also included. SD: standard deviation

	25 °C				45 °C	
	HD ± SD (nm)	**PDI ± SD**	**Zeta potential ± SD (mV)**	**r**	**HD ± SD (nm)**	**PDI ± SD**
DPPC:Ch:PEG 17:2:1	108.5 ± 7.9	0.238 ± 0.003	-22.89 ± 0.41	0.15	116.6 ± 1.3	0.245 ± 0.009
DPPC:PEG 19:1	193.8 ± 24.4	0.228 ± 0.008	-36.91 ± 0.68	0.17	145.8 ± 5.8	0.237 ± 0.006
DPPC:Ch:PEG 17:2:1 Lipogel	-	-	-	0.23	-	-
DPPC:PEG 19:1 Lipogel	-	-	-	0.22	-	-
Hydrogel	-	-	-	0.26	-	-

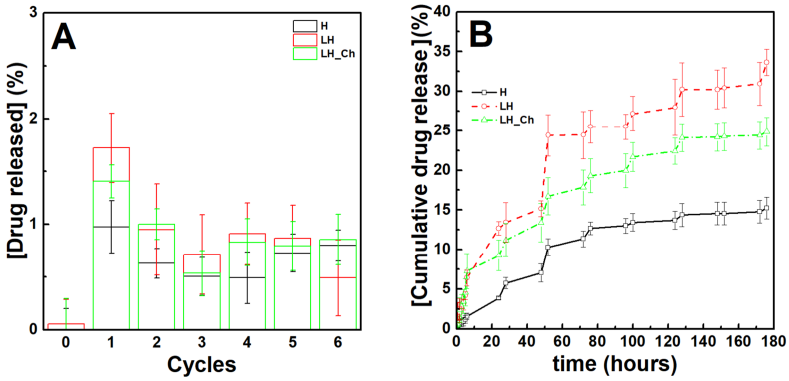

Figure S11. (A) Heat-triggered doxorubicin release per cycle from the hydrogel and lipogels containing DPPC:Ch:PEG 17:2:1 or DPPC:PEG 19:1. (B) Cumulative doxorubicin release from the hydrogel and lipogels containing DPPC:Ch:PEG 17:2:1 or DPPC:PEG 19:1 subjected to higher contribution from erosion at 25 °C. Each cycle of heating (45 °C) was carried out for 1 h with an interval of 24 h and the first cycle was initiated after 48 h of passive release. Legend: LH_Ch: Lipogel with DPPC:Ch:PEG 17:2:1 liposomes; LH: Lipogel with DPPC:PEG 19:1 liposomes; H: hydrogel.

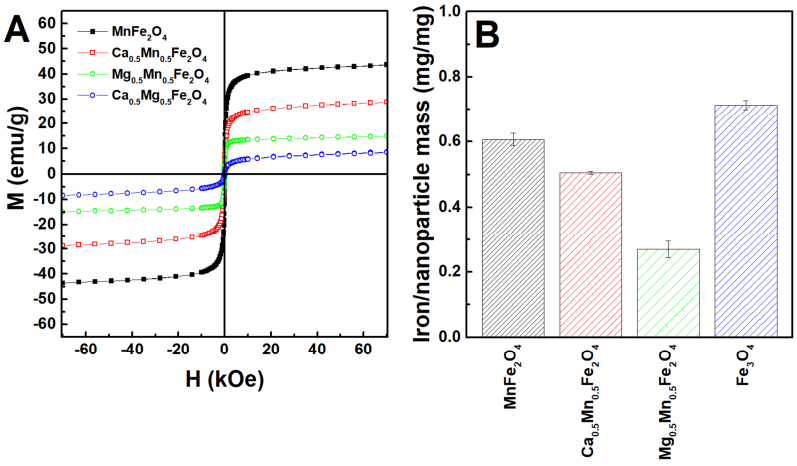

Figure S12. (A) Saturation of magnetization (Ms) of the synthesized nanoparticles (identified with the nominal synthesis stoichiometric values). (B) Iron mass per mass of nanoparticle of the samples with highest saturation of magnetization and comparison with iron content of magnetite obtained by the same method.

Table S2. Coercive field (H_c), saturation magnetization (M_s), remnant magnetization (M_r), and ratio M_r/M_s for calcium, magnesium and manganese doped ferrite nanoparticles (nominal synthesis stoichiometry), at room temperature (T=300 K), besides the mass of iron/nanoparticle (mg/mg) and the experimental iron stoichiometry estimate.

	H_c (Oe)	M_s (emu/g)	M_r (emu/g)	M_r/M_s	Iron/nanoparticle (mg/mg)	Iron stoichiometry
$MnFe_2O_4$	33	43.6	3.6	0.08	0.607 ± 0.019	2.55 ± 0.08
$Ca_{0.5}Mn_{0.5}Fe_2O_4$	12.0	28.7	0.4	0.01	0.509 ± 0.005	2.12 ± 0.02
$Mg_{0.5}Mn_{0.5}Fe_2O_4$	3.7	15.0	0.1	0.01	0.270 ± 0.026	1.13 ± 0.11
$Ca_{0.5}Mg_{0.5}Fe_2O_4$	34.3	8.7	0.2	0.02	-	-
Fe_3O_4	-	-	-	-	0.713 ± 0.014	3

X-ray diffraction parameters

A Rietveld analysis was performed using a phase adapted from a CIF file of iron oxide (CIF file 2300618) space group Fd-3m) by substituting iron by manganese (and calcium) with an inversion of 0.6 as reported for other manganese ferrites [8]. The diffraction peaks of the $MnFe_2O_4$ crystalline structure are observed at 2θ = 18.2 (1 1 1), 29.9° (2 2 0), 35.3° (3 1 1), 36.9° (2 2 2), 42.9° (4 0 0), 53.2° (4 2 2), 56.6° (3 3 3) and (5 1 1), 62.2° (4 4 0), 65.4° (5 3 1), 70.6° (6 2 0), 73.6° (5 3 3), 74.6° (6 2 2), 78.5° (4 4 4), 86.2° (6 4 2), 89.1° (7 3 1) and (5 5 3), and the diffraction peaks of the calcium-doped are at 2θ = 18.3 (1 1 1), 30.0° (2 2 0), 35.4° (3 1 1), 37.0° (2 2 2), 43.0° (4 0 0), 53.3° (4 2 2), 56.9° (3 3 3) and (5 1 1), 62.4° (4 4 0), 65.6° (5 3 1), 70.8° (6 2 0), 73.8° (5 3 3), 74.8° (6 2 2), 78.8° (4 4 4), 86.6° (6 4 2), 89.6° (7 3 1) and (5 5 3).

Table S3. X-ray diffraction Rietveld refinement calculated parameters Bragg R-factor (R_B) R_F-factor (R_F), χ^2 and phase sizes.

Nanoparticles	Phase size (nm)	Lattice Constant (Å)	R_F	R_B	χ^2
Manganese ferrite	9.20	8.433	4.54	4.72	0.90
Calcium-doped manganese ferrite	4.70	8.408	6.16	5.66	1.23

Raman analysis of (calcium-doped) manganese ferrite

The Raman spectra of ferrites is characterized by five major bands as predicted by the group theory for spinels with *Fd3m* space group: the A_{1g} band, E_g band, and three T_{2g} bands. Lorentzian curves were fitted to deconvolute the multiple contributions for each band (figure S14). The A_{1g} band is centered around 670 cm^{-1}, which displays a shoulder at ~715 cm^{-1} (band in orange) that can be associated with the presence of maghemite, cation vacancies or other order/disorder features [46,47].

The manganese ferrite additional A_{1g} band contributions stems from the distribution of Fe and Mn cations in the tetrahedral positions. Besides the band ~600 cm^{-1}, the contribution at ~640 cm^{-1} suggests the oxidation of some manganese cations to Mn^{3+} [46]. Doping with calcium led to additional contributions, which indicates the occupation of some sites by calcium cations.

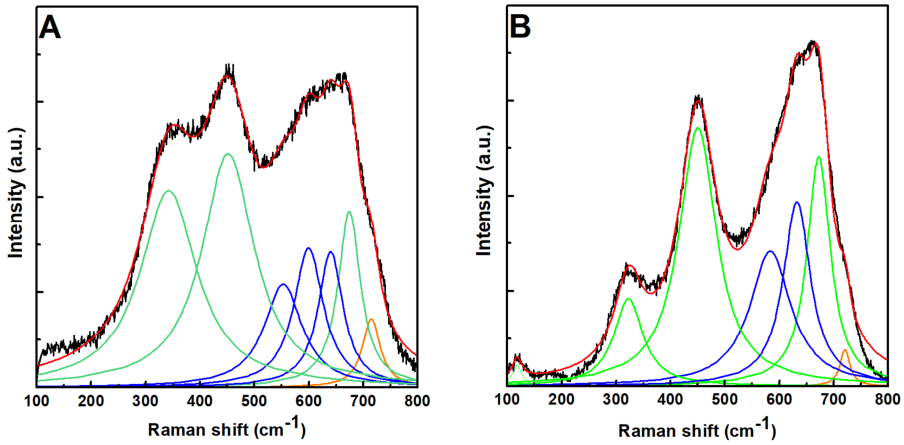

Figure S13. Raman scattering spectra of the (A) calcium-doped manganese ferrite and (B) manganese ferrite nanoparticles.

Functionalized nanoparticles magnetic properties

The Raman spectra of the functionalized nanoparticles display peaks which can be assigned to characteristic frequencies of phenylalanine, mainly associated with the side-chain C-C, N-C and CH_2 vibration modes, besides NH_3^+ symmetric bending and rocking (~1450 cm^{-1}) [48-51].

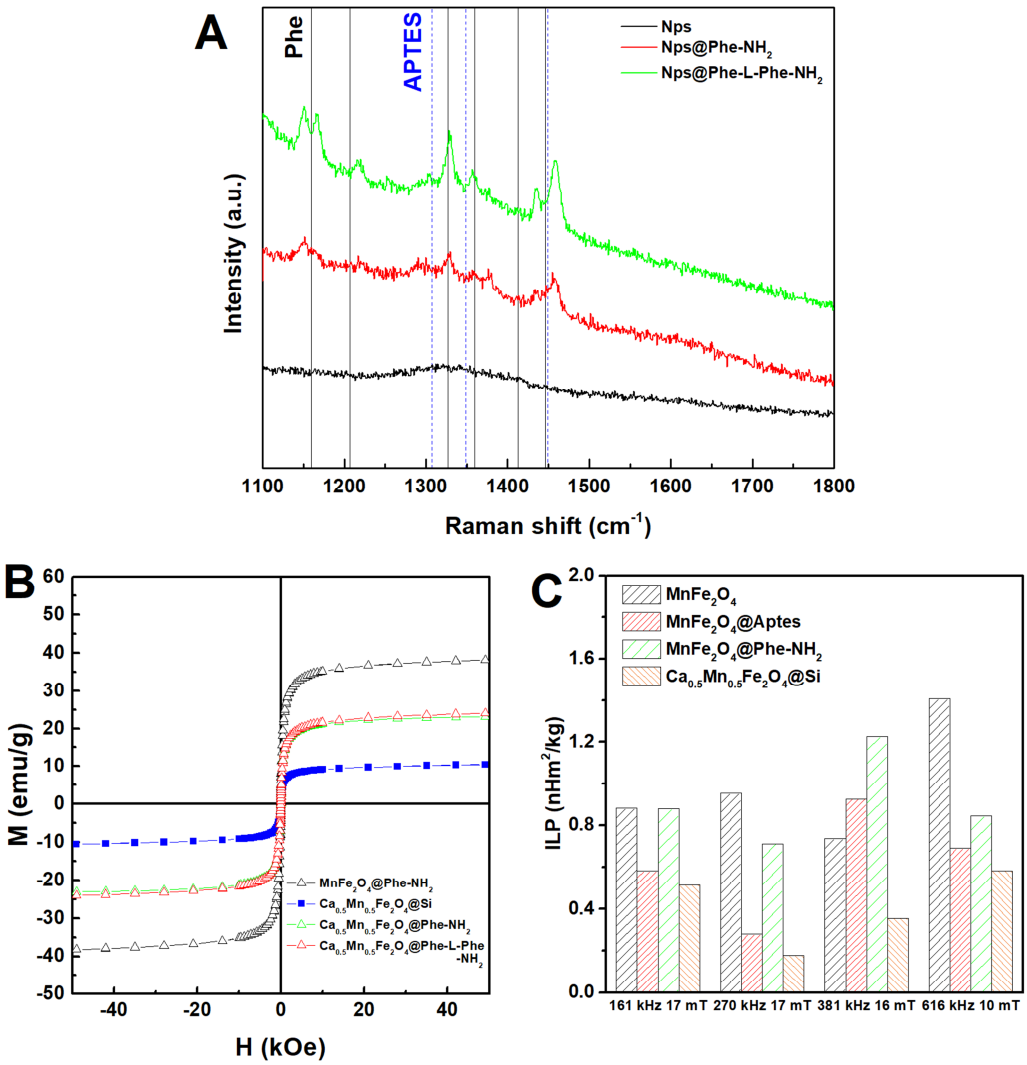

Figure S14. (A) Raman scattering spectra of the bare nanoparticles (Nps) and functionalized with phenylalanine (Nps@Phe-NH_2) and diphenylalanine (Nps@Phe-L-Phe-NH_2). The vertical lines represent the reported Raman shifts of phenylalanine (Phe, black) and APTES (blue). (B) Magnetization hysteresis loops of functionalized nanoparticles measured at room temperature (T=300 K) and silica coated calcium-doped manganese ferrite nanoparticles. (C) Intrinsic loss power (ILP) calculated from the temperature variation over time of functionalized manganese ferrite nanoparticles and silica coated calcium-doped manganese ferrite nanoparticles in water (1 mg/mL) under different magnetic field strengths and frequencies.

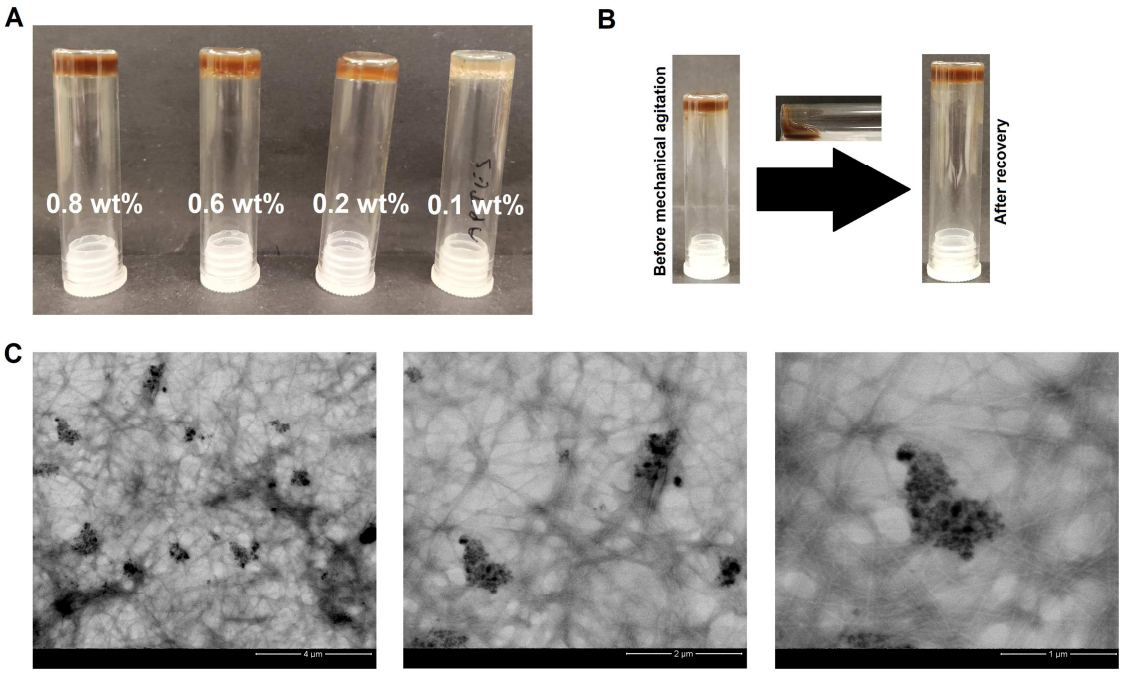

Figure S15. (A) Images of magnetic gels at different nanoparticle (calcium-doped manganese ferrite coated with APTES) content and (B) at high nanoparticle content (0.8 wt%) before and after breakage. (C) Transmission electron microscopy images at lower content (0.1 wt%) of nanoparticles. The gels we prepared with 0.5 wt% of hydrogelator and 0.4 wt% of GdL.

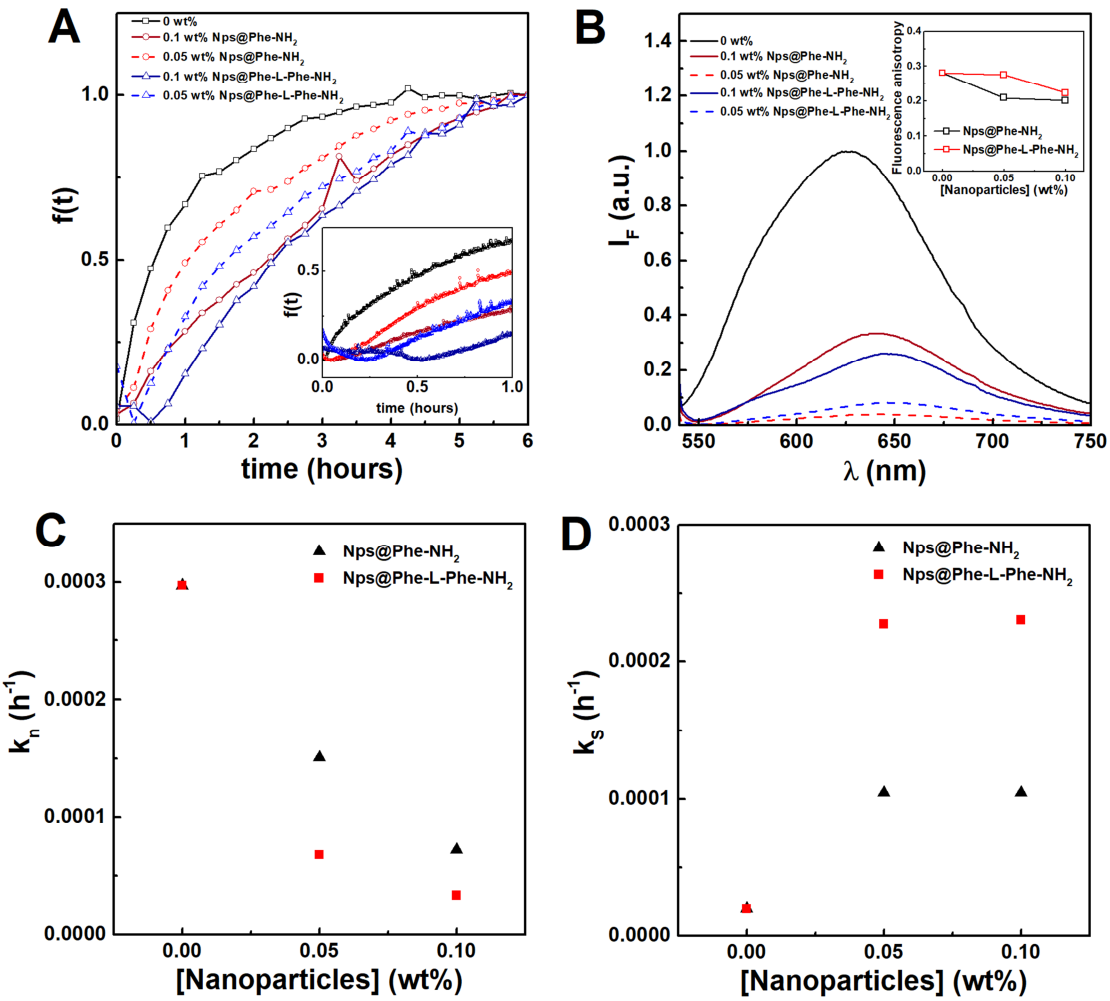

Figure S16. (A) Fluorescence emission kinetics of gel loaded with Nile Red (2 μM, λ_{exc}=520 nm, λ_{em}=620 nm) and various concentrations of functionalized nanoparticles. Inset: first hour of the gelation kinetics. The initial decrease of fluorescence emission in the lag phase can be associated with the assembly between nanoparticles and fibres, which is not observed in neat gels or lipogels. (B) Fluorescence emission of Nile Red (2 μM, λ_{exc}=520 nm, λ_{em}=620 nm) in gels with various concentrations of functionalized nanoparticles. Inset: Nile Red fluorescence anisotropy dependence on the particles' concentration. (C,D) Kinetic parameters obtained from the fitting of the Saitô's fractional aggregation model to the fluorescence kinetics data. The parameter k_s is the effective growth rate, and k_n is the nucleation rate.

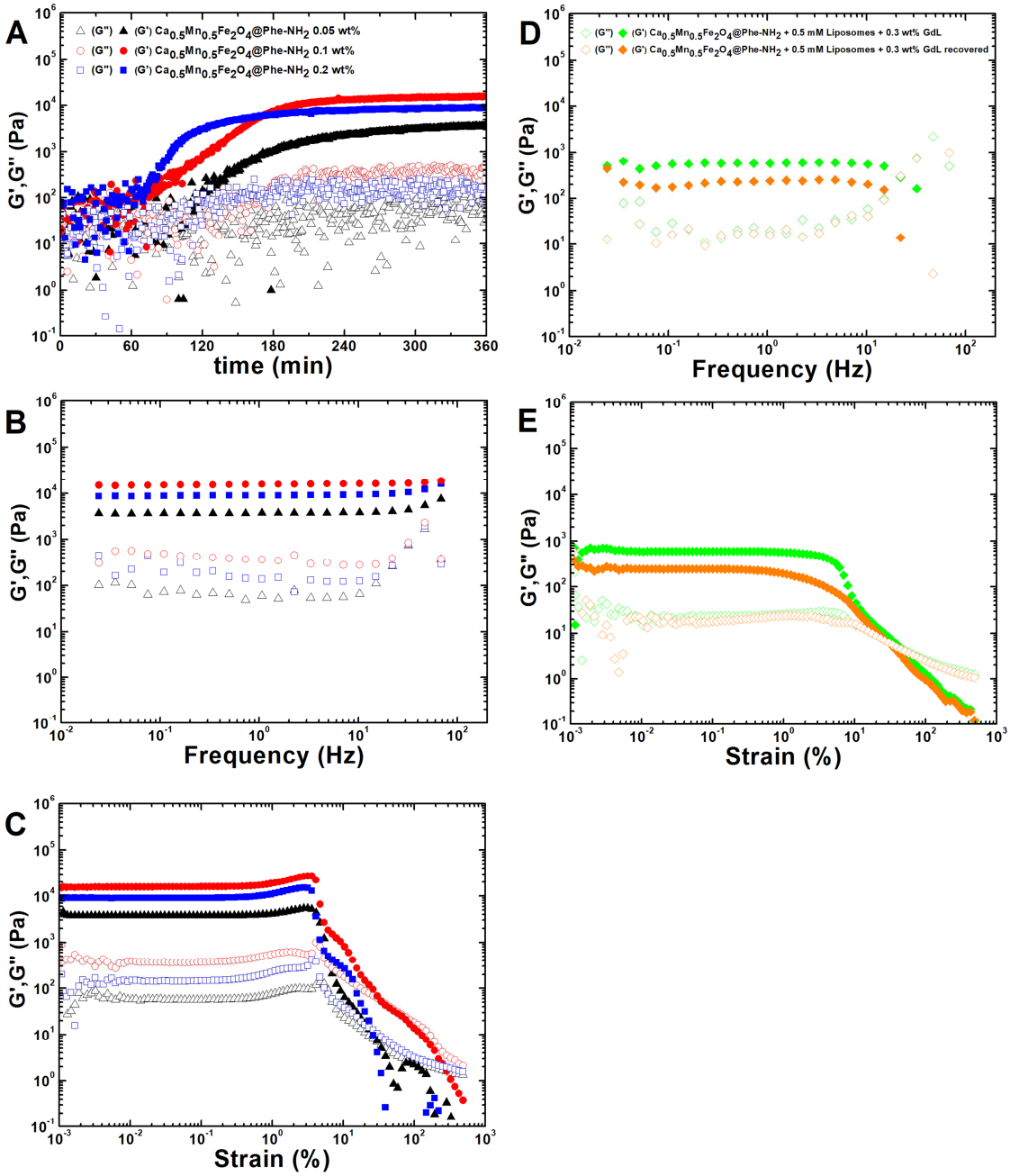

Figure S17. (A) Shear storage G' (filled symbols) and loss G'' (empty symbols) modulus during the kinetic process of gelation, (B) frequency sweep and (C) strain sweep of magnetogels (0.5 wt% hydrogelator; 0.4 wt% GdL) bearing manganese ferrite nanoparticles coated with phenylalanine ($MnFe_2O_4$@Phe-NH_2) at different concentration (0.05 wt%, 0.1 wt% and 0.2 wt%). (D,E) Shear storage G' (filled symbols) and loss G'' (empty symbols) modulus dependence during frequency and strain sweep before and 3 hours after breaking (recovered) of magnetogels (0.5 wt% hydrogelator, 0.3 wt% GdL) prepared with 0.1 wt% of calcium-doped manganese ferrites coated with phenylalanine and 0.5 mM of liposomes.

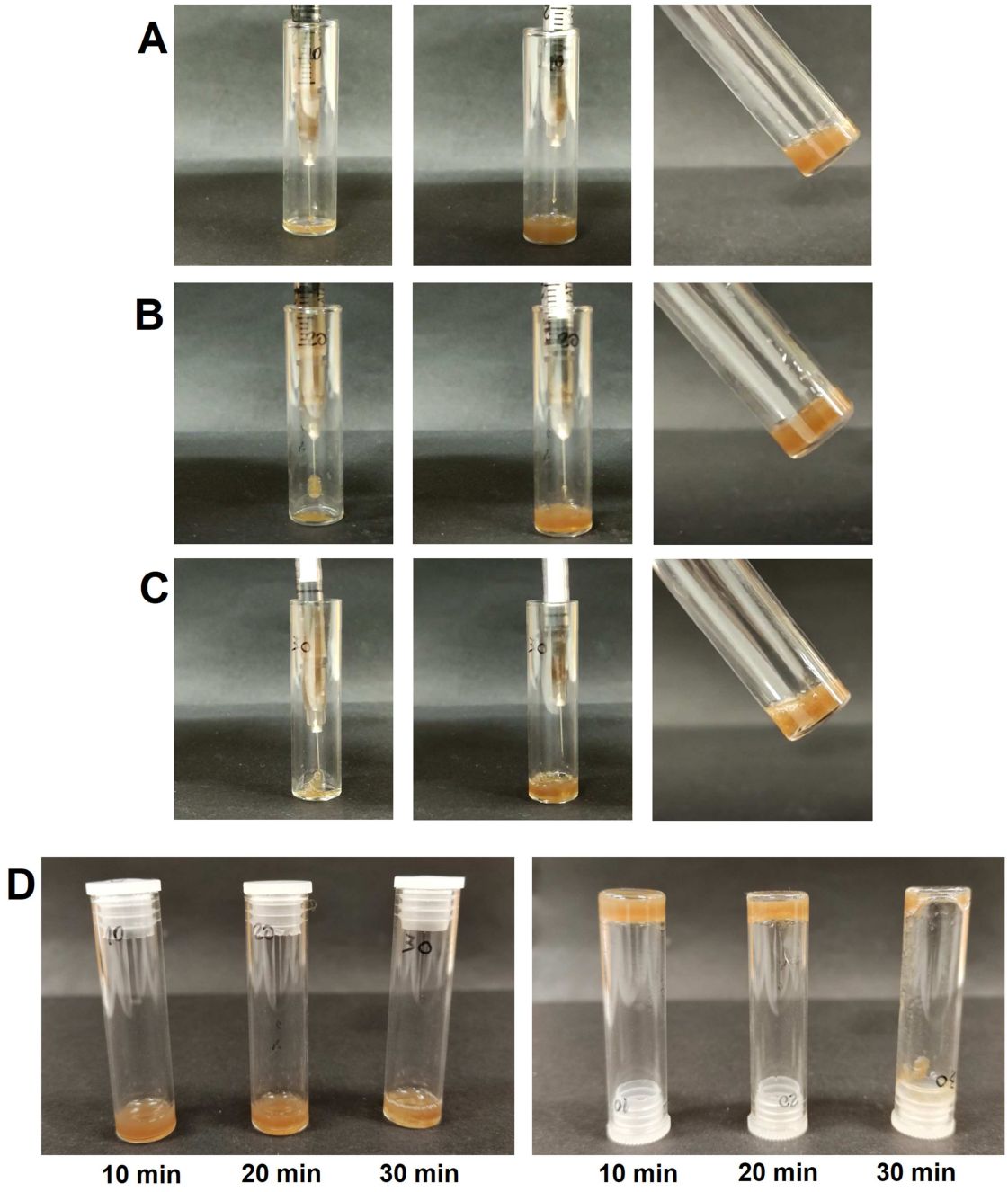

Figure S18. (A,B,C) Sequential images of the magnetogel injection at 10, 20 and 30 min after inducing gelation. (D) Vial inversion of injected magnetic gel solutions 35 min post-triggered gelation. Despite the sample B forming a gel it displayed some inhomogeneities, while the sample A was homogeneous. The sample C displayed phase separation between water and gel after injection.

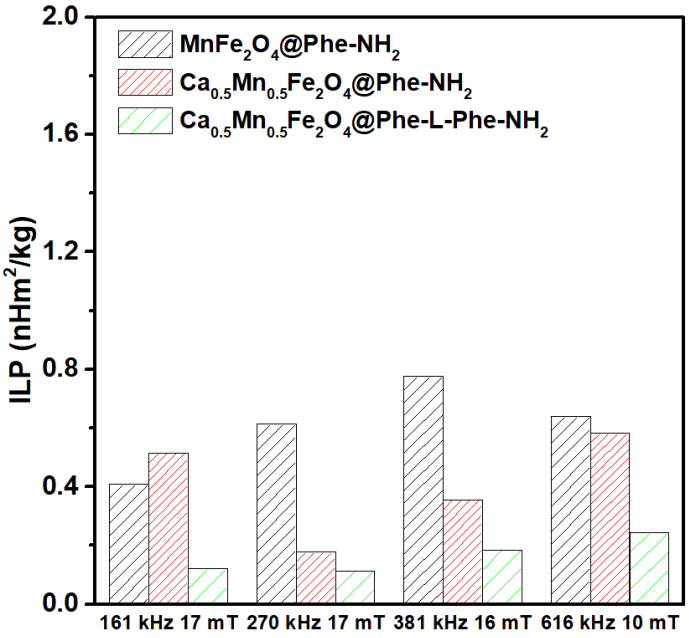

Figure S19. Intrinsic loss power (ILP) calculated from the temperature variation over time of functionalized nanoparticles (1 mg/mL) in gels (0.5 wt% hydrogelator, 0.4 wt% GdL) under different magnetic field strengths and frequencies.

Passive and active doxorubicin release

Table S4. Coefficients of determination (R^2) obtained for doxorubicin release profiles (0.1 mM) in magneto(lipo)gels with different composites. The blank spaces correspond to negative coefficients.

System	Particle	First-order	Hixson-Crowell	Higuchi	Korsmeyer-Peppas	Gompertz
Hydrogel	-	0.67	0.52	0.92	0.97	0.99
Lipogel	-	0.85	0.49	0.94	0.96	0.99
Magnetogel	0.1 wt% $Ca_{0.5}Mn_{0.5}Fe_2O_4$@Phe-NH_2	0.77	-	0.88	0.95	0.99
	0.3 wt% $Ca_{0.5}Mn_{0.5}Fe_2O_4$@Phe-NH_2	0.78	-	0.88	0.96	0.99
	0.1 wt% $Ca_{0.5}Mn_{0.5}Fe_2O_4$@Phe-L-Phe-NH_2	0.81	-	0.92	0.97	0.99
	0.3 wt% $Ca_{0.5}Mn_{0.5}Fe_2O_4$@Phe-L-Phe-NH_2	0.74	-	0.80	0.96	0.99
	0.1 wt% $MnFe_2O_4$@Phe-NH_2	0.66	-	0.61	0.93	0.98
Magnetolipogel	0.1 wt% $Ca_{0.5}Mn_{0.5}Fe_2O_4$@Phe-NH_2	0.81	-	0.88	0.95	0.97
	0.1 wt% $Ca_{0.5}Mn_{0.5}Fe_2O_4$@Phe-L-Phe-NH_2	0.66	-	0.55	0.94	0.99
	0.1 wt% $MnFe_2O_4$@Phe-NH_2	0.66	-	0.68	0.92	0.98

The Gompertz and Korsmeyer-Peppas models are described according to the equations:

$$X_t = X_{max} e^{-ae^{b \log_{10} t}} \quad \text{(S1)}$$

$$C_t = C_0 K_s t^n \quad \text{(S2)}$$

where X_t and X_{max} are the dissolved fractions at time *t* and its maximum, a is a shape parameter and b is the dissolution rate per unit of time [62]. The C_0 and C_t are the concentrations at time 0 and *t*, and K_s is the rate constant. When $n < 0.45$, the release mechanism is diffusion-controlled (Fickian release), $0.45 < n < 0.89$ indicates a combination of diffusion and erosion drug release (non-Fickian release), $0.89 < n < 1$ indicates a relaxation-controlled release, and if $n > 1$, the release is controlled by swelling and polymer chain relaxation [62,63].

Table S5. Release coefficients of the Korsmeyer-Peppas model obtained for doxorubicin release profiles (0.1 mM) in magneto(lipo)gels with different composites.

		Korsmeyer-Peppas			Gompertz			
Drug	**Hydrogel**	K_S	n	R^2	X_{max}	a	b	R^2
Hydrogel	-	0.00648	0.41	0.97	0.05	2.46	0.82	0.99
Lipogel	-	0.00687	0.48	0.96	0.06	2.89	1.14	0.99
Magnetogel	0.2 wt% $Ca_{0.5}Mn_{0.5}Fe_2O_4$@Phe-NH_2	0.00604	0.39	0.95	0.03	2.19	1.26	0.99
	0.3 wt% $Ca_{0.5}Mn_{0.5}Fe_2O_4$@Phe-NH_2	0.00282	0.38	0.96	0.02	2.21	0.94	0.99
	0.2 wt% $Ca_{0.5}Mn_{0.5}Fe_2O_4$@Phe-L-Phe-NH_2	0.00413	0.41	0.97	0.03	2.40	0.90	0.99
	0.3 wt% $Ca_{0.5}Mn_{0.5}Fe_2O_4$@Phe-L-Phe-NH_2	0.00432	0.34	0.96	0.02	1.86	0.99	0.99
	0.1 wt% $MnFe_2O_4$@Phe-NH_2	0.00181	0.29	0.93	0.01	1.68	0.81	0.98
Magnetolipogel	0.2 wt% $Ca_{0.5}Mn_{0.5}Fe_2O_4$@Phe-NH_2	0.00509	0.39	0.95	0.04	2.40	0.73	0.97
	0.2 wt% $Ca_{0.5}Mn_{0.5}Fe_2O_4$@Phe-L-Phe-NH_2	0.01021	0.28	0.94	0.03	1.44	1.10	0.99
	0.2 wt% $MnFe_2O_4$@Phe-NH_2	0.00245	0.31	0.92	0.01	1.66	1.40	0.98

Table S6. Release coefficients of the Korsmeyer-Peppas model obtained for doxorubicin release profiles (0.1 mM) in magneto(lipo)gels with different composites for the first 6h of drug release.

		Korsmeyer-Peppas		
Drug	**Hydrogel**	K_S	n	R^2
Hydrogel	-	0.00477	0.66	0.99
Lipogel	-	0.00416	0.86	0.99
Magnetogel	0.3 wt% $Ca_{0.5}Mn_{0.5}Fe_2O_4$@Phe-NH_2	0.00395	0.76	0.99
	0.3 wt% $Ca_{0.5}Mn_{0.5}$ Fe_2O_4@Phe-NH_2	0.00209	0.63	0.99
	0.3 wt% $Ca_{0.5}Mn_{0.5}$ Fe_2O_4@Phe-L-Phe-NH_2	0.00305	0.67	0.99
	0.3 wt% $Ca_{0.5}Mn_{0.5}$ Fe_2O_4@Phe-L-Phe-NH_2	0.00336	0.59	0.99
	0.1 wt% $MnFe_2O_4$@Phe-NH_2	0.00145	0.52	0.99
Magnetolipogel	0.3 wt% $Ca_{0.5}Mn_{0.5}Fe_2O_4$@Phe-NH_2	0.00360	0.70	0.99
	0.3 wt% $Ca_{0.5}Mn_{0.5}Fe_2O_4$@Phe-L-Phe-NH_2	0.00806	0.52	0.99
	0.3 wt% $MnFe_2O_4$@Phe-NH_2	0.00176	0.62	0.99

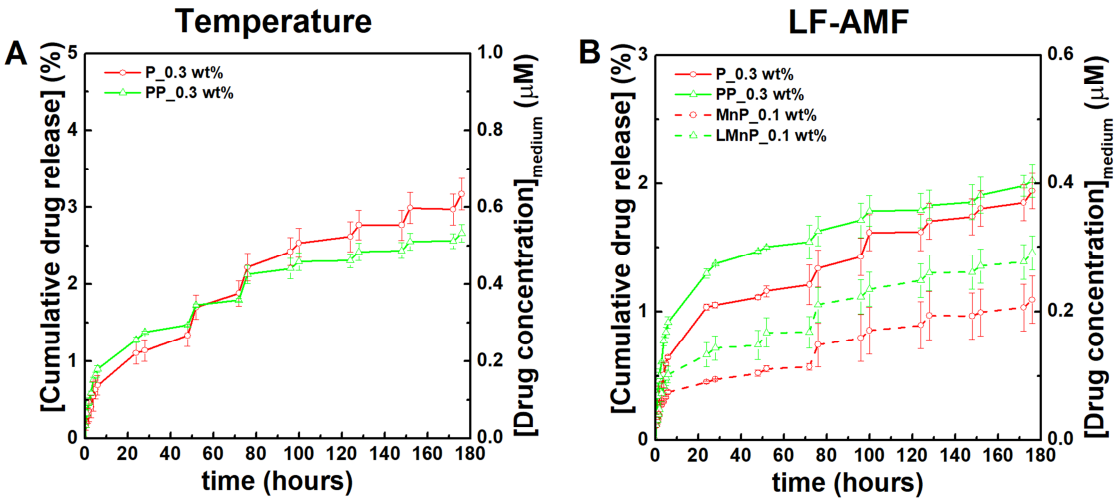

Figure S20. Cumulative doxorubicin release from magnetogels containing phenylalanine (P) and diphenylalanine (PP) functionalized calcium-doped manganese ferrite nanoparticles (0.3 wt%) to phosphate buffer pH=7.4, and from magneto(lipo)gels ((L)MnP) containing phenylalanine functionalized manganese ferrite nanoparticles (0.1 wt%). The gels were subjected either to a heating cycle (45 °C) carried out for 1 h with an interval of 24 h or a low-frequency magnetic field (LF-AMF) for 2 hours. The first cycle was initiated after 48 h of passive release. The concentration of doxorubicin in gels is 100 µM, and the maximum that can be accumulated in the medium is 20 µM (200 µL gel for 800 buffer medium).

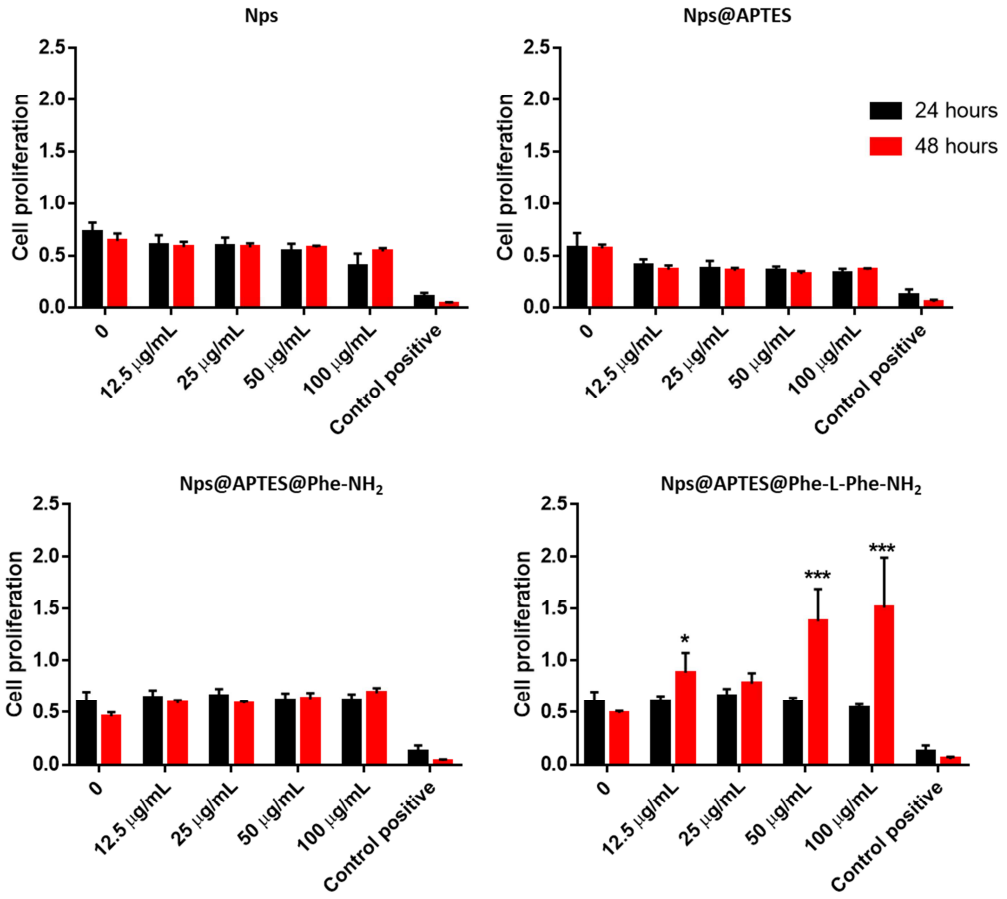

Figure S21. In vitro cell proliferation assays of magnetic nanoparticles with the core of calcium-doped manganese ferrite (Nps) functionalized with APTES, phenylalanine and diphenylalanine performed with human neuroblastoma cell line SH-SY5Y by the MTT assay. Data is represented as mean ± SD, and n = 12. *Denotes significant difference between sample and control groups ($p < 0.05$).

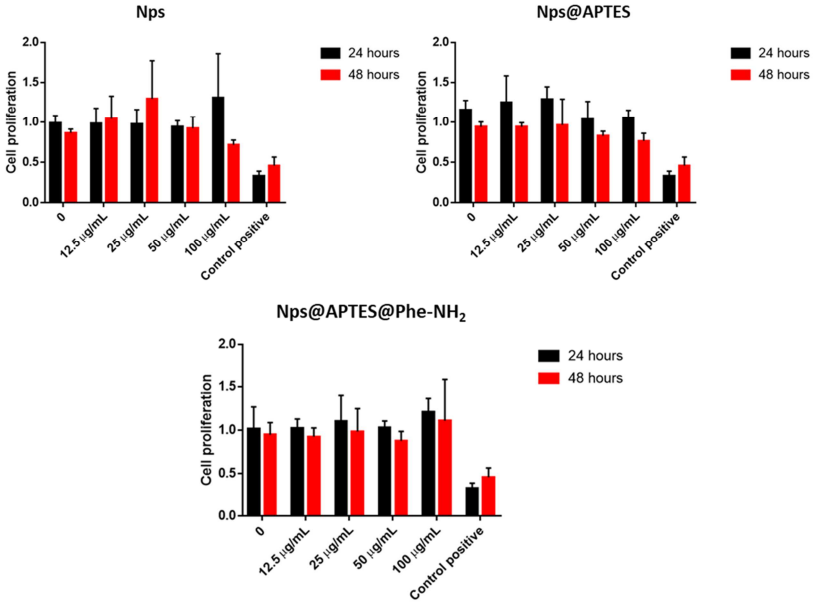

Figure S22. In vitro cell proliferation assays of magnetic nanoparticles with the core of manganese ferrite (Nps) functionalized with APTES and phenylalanine performed with human glioblastoma cell line U251 by the MTT assay. Data is represented as mean ± SD, and n = 12. *Denotes significant difference between sample and control groups ($p < 0.05$).

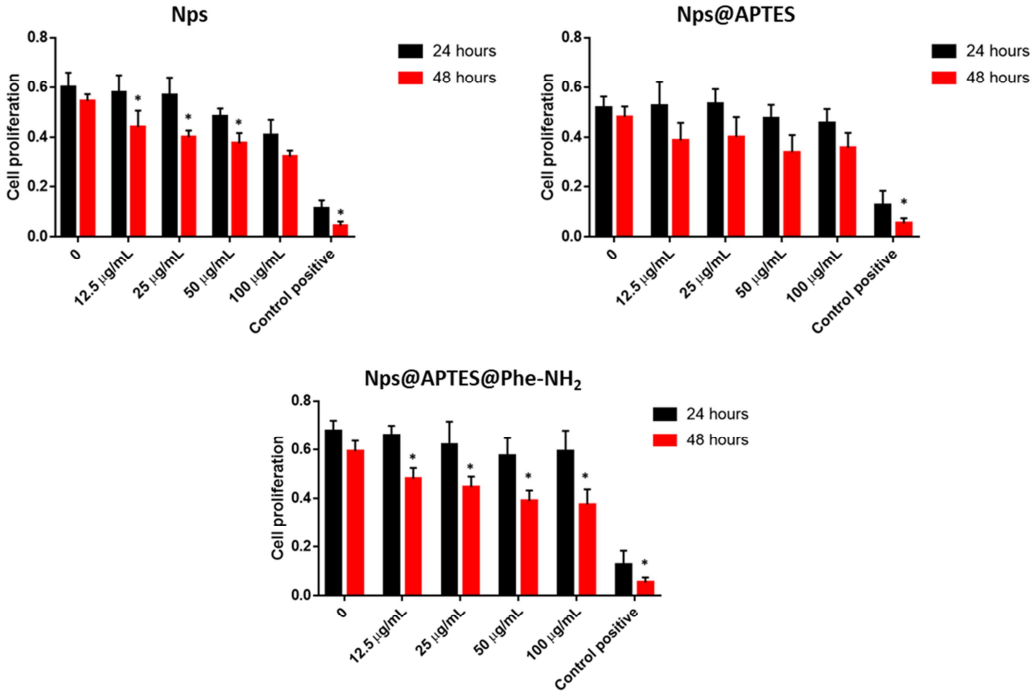

Figure S23. In vitro cell proliferation assays of magnetic nanoparticles with the core of manganese ferrite (Nps) functionalized with APTES and phenylalanine performed with human neuroblastoma cell line SH-SY5Y by the MTT assay. Data is represented as mean ± SD, and n = 12. *Denotes significant difference between sample and control groups ($p < 0.05$).